ParaMaster: Design and Experimental Characterizations of a Haptic Device for Surgical Teleoperation

Xu Liu, Baibo Wu, Zhonghao Wu, Lingyun Zeng, and Kai Xu*, *Member, IEEE*

Abstract—A multi-DoF (Degrees of Freedom) haptic device is a crucial module in a teleoperation-based surgical robotic system. Numerous haptic devices have been developed for a surgeon to teleoperate slave surgical manipulators. However, these research prototypes can be arduous to reproduce outside the original lab, while the commercially available products are often quite expensive. To fulfill the need of affordable haptic devices for a teleoperated laparoscopic surgical system, a new master haptic device, the ParaMaster, with a parallelogram structure, is proposed in this study. The ParaMaster design is based on affordable direct drive motors and with 6-DoF inputs and 6-DoF outputs. The design concept, kinematics, dimension optimization, gravity compensation, design description and preliminary experimental verifications are elaborated. The ParaMaster is expected to be integrated into a laparoscopic surgical system after receiving full calibrations of its motion sensing and wrench outputs capabilities in the near future.

I. INTRODUCTION

MASTER-SLAVE teleoperation is the most commonly adopted form in many surgical robotic systems. Each system usually include a master console and multiple multi-DoF (Degree of Freedom) patient-side slave surgical manipulators [1]. One pair of haptic devices are often installed at the master console for a surgeon to teleoperate the slave surgical manipulators to perform surgical treatments. Besides sensing the position and orientation of the operator's hand, the master haptic device should preferrably generate force and torque outputs, e.g., providing haptic feedback to the operator [2]. Furthermore, the force and torque outputs can be used for assistive functions such as the hand trembling damping control and setting forbidden regions, which can increase the safety of a surgical robotic system [3]. Accuracy, dexterity, low friction and low inertia are all important design considerations for hapic devices [4].

Due to the various needs of haptic devices, different device types have therefore been developed. In accordance with their input and output capabilities, the existing haptic devices can be categorized as follows: 3-in-3-out devices, 6-in-3-out devices and 6-in-6-out devices.

Most 3-in-3-out haptic devices sense 3-DoF position inputs and generate 3-DoF force outputs. The examples include the delta.3 and the omega.3 devices (Force Dimension, Inc.), the DELTA-R device [5], etc.

6-in-3-out haptic devices sense 6-DoF inputs (including positions and orientations), and mostly generate force outputs. The examples include the Touch device (3D Systems, Inc.), the omega.6 device (Force Dimension, Inc.), and the laparoscopic interface in [6].

6-in-6-out haptic devices can sense 6-DoF inputs and generate 6-DoF wrench outputs (including forces and torque components). The examples include the sigma.7 device (Force Dimension, Inc.), the PATHOS-II device [7], the haptic cobot [8], the CU haptic interface [9], and the VirtuaPower device [10].

6-in-6-out haptic devices are highly preferred in teleoperation-based surgical robotic systems because the wrench outputs can greatly facilitate a quick establishment of the pose mapping between the stylus of the haptic device and the end effector of different remote surgical manipulators [11]. However, the 6-in-6-out products are indeed expensive, while the state-of-the-art research prototypes cannot be conveniently reproduced outside the original labs. To fulfil the need of affordable haptic devices for a teleoperated laparoscopic surgical system, a new 6-in-6-out master haptic device, the ParaMaster, with a parallelogram structure, is proposed as shown in Fig. 1.
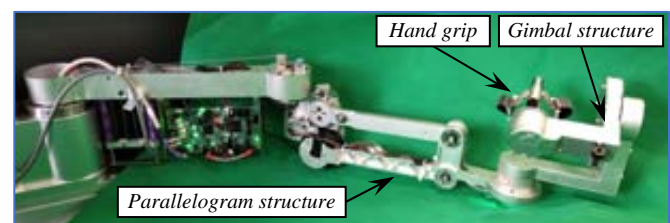

Fig. 1. The constructed ParaMaster haptic device

The ParaMaster design is based on affordable direct drive motors and possesses 6-DoF inputs and 6-DoF outputs.

The first three revolute joints, using a parallelogram structure, provide 3-DoF translation motions of a 3-DoF gimbal structure. Axes of the three joints of the gimbal structure intersect at a point. What's more, a stylus with a 1-DoF hand grip is installed to sense the open and close commands from the operator for the surgical end effector.

The ParaMaster was designed to possess a large workspace such that a motion scaling control during teleoperation is easier. The direct drive motors are adopted to eliminate

backlashes and reduce the viscosity and the friction from a gear transmission.

The rest of this paper is organized as follows. Section II explains the design concept of the ParaMaster device, while the kinematics modeling, dimension optimization and gravity compensation design are elaborated in Section III. Section IV reports the ParaMaster's design descriptions. Preliminary experimental verifications are reported in Section V, with the conclusions and future works summarized in Section VI.

II. DESIGN CONCEPT

To make sure the ParaMaster has a large workspace that can cover the target operation region (a $500 \times 190 \times 300$ mm^3 cube) while keeping a relatively compact structure, a serial structure is selected.

Since the ParaMaster possesses six DoFs, the first three DoFs were intended to realize the translation motions of the 3-DoF gimbal structure. However, the gravity compensation for a serial linkage with multiple joints can be challenging. In order to minimize the influence of the gravity, axes of the first and second joints were chosen to be vertical, as shown in Fig. 2. A parallelogram structure with the third active joint and three passive joints was used to realize vertical translation motions. The use of the parallelogram brings two major advantages as follows. Firstly, the torque exerted on the third active joint is from the mass of the gimbal structure. This eases the gravity compensation design as detailed in Section III.D. Secondly, the untilted vertical translation facilitates the inverse kinematics.

The gimbal structure can orient the stylus with a hand grip integrated. The hand grip is programmed to sense the open and close angle to control the end effector (e.g., a needle driver) of the remote surgical manipulator. Because the gimbal structure is kept untilted while being translated by the first three joints of the ParaMaster device, only the fifth active joint should be designed for gravity compensation within the gimbal structure.
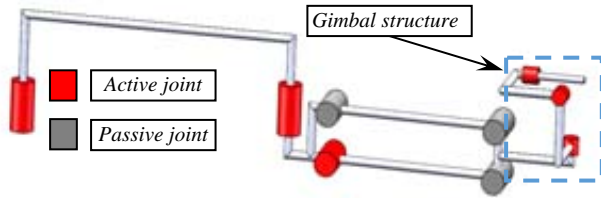

Fig. 2.   The scheme of the ParaMaster

III. MODELING, OPTIMIZATION AND GRAVITY BALANCE

Nomenclature and coordinate systems for the ParaMaster are first defined in Section III.A, while the kinematics is derived in Section III.B. Dimension optimization for the ParaMaster is presented in Section III.C, while the gravity compensation design is elaborated in Section III.D.

A. Nomenclature and Coordinate Systems

As shown in Fig. 3, the following coordinate systems are defined for the ParaMaster's kinematics.

- *The base coordinate $\{D_0\} \equiv \{\hat{\mathbf{x}}_0, \hat{\mathbf{y}}_0, \hat{\mathbf{z}}_0\}$ locates its origin at the center of the base cross section with $\hat{\mathbf{z}}_0$ perpendicular to the base cross section.*

- *The ParaMaster coordinate $\{D_i\} \equiv \{\hat{\mathbf{x}}_i, \hat{\mathbf{y}}_i, \hat{\mathbf{z}}_i\}$ ($i = 1, 2, 2'$, 3..., 6) are assigned to the ith link or the stylus of the ParaMaster following the Denavit-Hartenberg (the D-H) convention.*
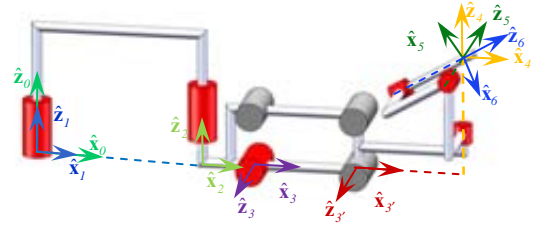

Fig. 3.Nomenclature and coordinates of the ParaMaster

TABLE I.
THE D-H PARAMETER OF THE PARAMASTER

Index i	α_{i-1} (rad)	a_{i-1} (mm)	d_i (mm)	θ_i (rad)
1	0	0	0	q_1
2	0	$a_1 = 350$	0	q_2
3	$\pi/2$	$a_2 = 55$	0	q_3
3'	0	$a_3 = 220$	0	$q_{3'} = -q_3$
4	$-\pi/2$	$a_3' = 95$	140	q_4
5	$-\pi/2$	0	0	$-\pi/2 + q_5$
6	$-\pi/2$	0	0	q_6

B. Kinematics

With the nomenclature and the coordinates defined, the kinematics of the ParaMaster can be formulated as follows.

$$^0\mathbf{T}_6 = \prod {}^{i-1}\mathbf{T}_i \quad i = 1, 2, \cdots, 6 \tag{1}$$

Where $^{i-1}\mathbf{T}_i = \mathbf{T}_{rot}(\mathbf{x}, \alpha_{i-1})\mathbf{T}_{trans}(\mathbf{x}, a_{i-1})\mathbf{T}_{trans}(\mathbf{z}, d_i)\mathbf{T}_{rot}(\mathbf{z}, \theta_i)$ is the homogeneous transformation matrix between $\{D_i\}$ and $\{D_{i-1}\}$, formulated using the D-H parameters; $\mathbf{T}_{rot}(\mathbf{n}, \gamma)$ and $\mathbf{T}_{trans}(\mathbf{m}, \eta)$ represent the rotation γ around the $\mathbf{n}$ axis, and the translation η around the $\mathbf{m}$ axis.

The ParaMaster's D-H parameters are listed in Table I.

The inverse kinematics of the ParaMaster is derived as follows. The homogeneous transformation matrix linking $\{D_0\}$ and $\{D_6\}$ can be written as in (2).

$$^0\mathbf{T}_6 = \begin{bmatrix} {}^0\mathbf{R}_6 & {}^0\mathbf{p}_6 \\ \mathbf{0} & 1 \end{bmatrix} \tag{2}$$

Where $^0\mathbf{p}_6 = {}^0\mathbf{p}_4$ due to the fact that the gimbal structure has its axes intersected at one point. The variables q_1, q_2 and q_3 corresponding to $^0\mathbf{p}_4$ can be easily obtained because of the serial structure of the first three joints. Then the rotation matrix $^0\mathbf{R}_{3'}$ of $^0\mathbf{T}_{3'}$ linking $\{D_0\}$ and $\{D_{3'}\}$ is calculated using q_1, q_2 and q_3. The orientation of the gimbal structure with respect to $\{D_{3'}\}$ can be determined from (3) as in (4).

$$^0\mathbf{R}_6 = {}^0\mathbf{R}_{3'} \, {}^{3'}\mathbf{R}_6 \tag{3}$$

$$^0\mathbf{R}_{3'}^T \, {}^0\mathbf{R}_6 = {}^{3'}\mathbf{R}_6 \tag{4}$$

Two sets of solutions can be derived from (4). One set is excluded by limiting q_4 to $(-\pi/2, \pi/2]$.

C. Dimension Optimization

As illustrated in Fig. 4(a), a pair of the ParaMasters is intended to be symmetrically arranged on a master console. An optimization for the linkage lengths were carried out. Since the size of the translational workspace is not affected by the gimbal structure, the optimization problem is hence simplified as minimizing the lengths of the linkages that provide the translational motions.
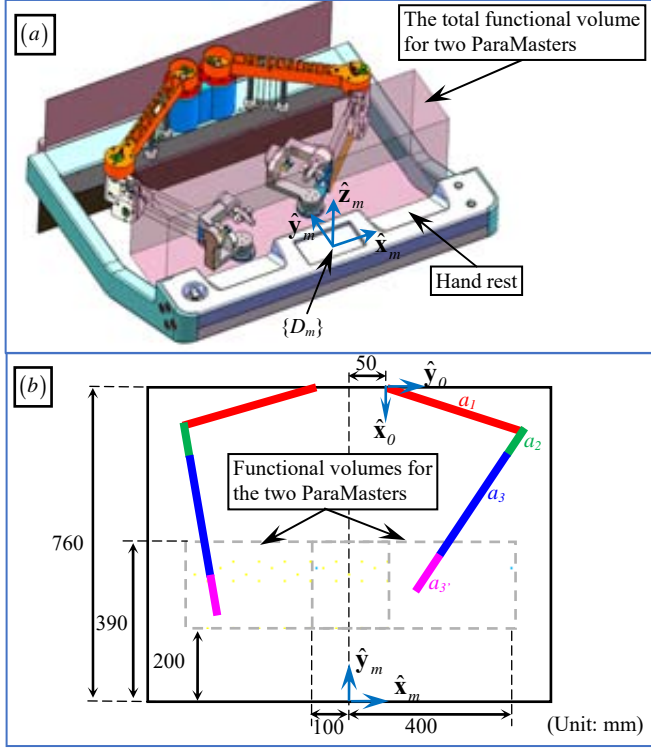

Fig. 4. The arrangement of the ParaMasters on the master console: (a) the CAD model showing the functional volume of the two ParaMasters, and (b) the top-view diagram of the console.

The master console coordinate $\{D_m\}$ fixed to the hand rest bar is used as the reference coordinate. Based on the ergonomics of the console design, two functional volumes for each ParaMaster with a size of $500 \times 190 \times 300 \text{ mm}^3$ are targeted in the central region of the console. The position of the functional volume is in Fig. 4(b). The volume is symmetric with respect to the XY-plane of $\{D_m\}$. The bases of the ParaMasters are located 760 mm from $\{D_m\}$ in the Y-direction, and are separated from each other by 100 mm to accommodate the base actuations. The vertical position of the ParaMaster's base is placed such that $\{D_6\}$ is in the XY-plane of $\{D_m\}$ when $q_3 = 0$. Since the size of the translational workspace is not influenced by the gimbal structure, the workspace of the ParaMaster is obtained by investigating the movements of the first three active joints.

The link lengths a_2 and a_3 are preset as 55 mm and 95 mm, based on the requirements of the mechanical design of the joints. The optimization objective is hence to minimize the total lengths of link 1 and link 3. The two ParaMasters are different in their joint motion ranges. Because of symmetry, the optimization problem for the right ParaMaster is

presented, as in (5).

$$\min\{a_1 + a_3\} \quad w.r.t \begin{cases} q_1 \in [0, \pi/2], q_2 \in [-\pi, 0] \\ q_3 \in [-\pi/4, \pi/4] \\ V_{func} \subseteq V_{reach} \end{cases} \quad (5)$$

The first constraint on q_1 is proposed to avoid the mutual collision of the two ParaMasters with each other and with the console, while the second constraint on q_2 is used to select the elbow-up solution. The third constraint on q_3 aims to limit the motion range to spare the room for the implementation of the gravity compensation discussed in Section III.D. V_{func} is the functional volume, and V_{reach} is the set of all the possible positions that can be reached by $\{D_6\}$.
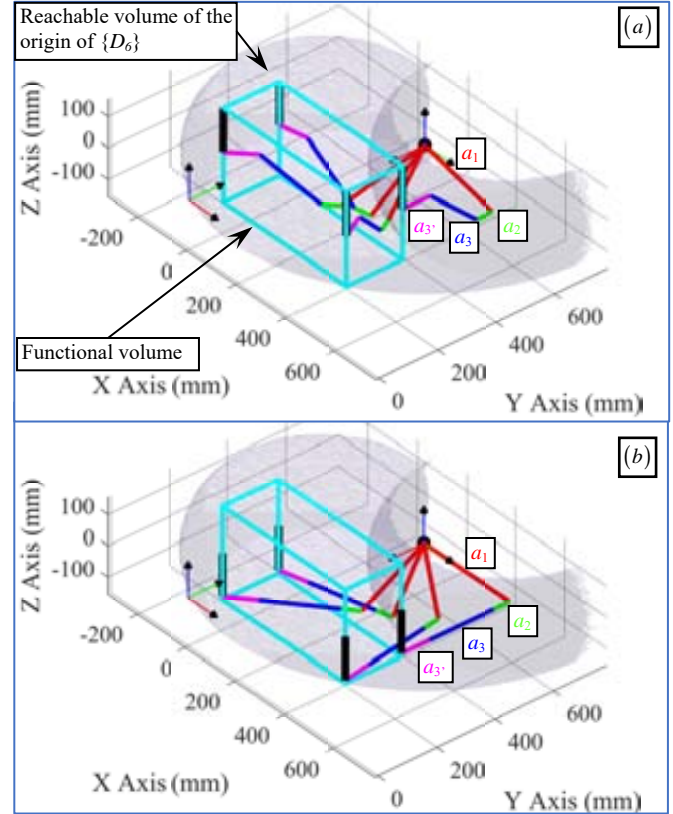

Fig. 5. The configurations for reaching: (a) the middle of the vertical edges, and (b) the upper vertices

An enumerative approach was adopted for this optimization. Firstly, the variables a_1 and a_3 were varied from 100 mm to 600 mm with an increment of 1 mm. For each pair of the enumerated values, the constraints in (5) is checked for validity. The inverse kinematics problems were solved by commanding the ParaMaster to reach discrete positions along the 12 edges of the functional volume with an 1 mm interval; The solutions were then checked if they were in the valid joint motion ranges from (3).

The optimized result was obtained as $a_1 = 350$ mm and $a_3 = 220$ mm. As shown in Fig. 5, the reachable volume V_{reach} corresponding to the optimized parameters is generated via the forward kinematics using random values sampled from

the joint space. Several typical configurations for reaching the vertices on the middle and top plane of the functional volume are plotted.

D. Gravity Compensation Design of the Parallelogram

As mentioned in Section II, the torques on the third and the fifth joints would be affected by gravity and it is preferred that the gravity-caused torques can be balanced.

Because the gimbal structure is kept untilted due to the parallelogram structure, the gravitational torque on the fifth joint can be cancelled regardless of the motions of the first three joints, referring to Fig. 7. Then, the torque on the fifth joint, caused by the weight of the sixth joint, can be easily balanced by attaching a counterweight on the fifth link, as shown in Fig. 7. The increased inertia is within the acceptable range. The weight of the counterweight is calculated from the CAD model. Even though the counterweight is not perfectly accurate, the residual gravity-casued torque is well within the torque capacity of the direct drive motor in the fifth joint.

While refining the gravity balance design of the third active joint, it will be nearly impossible to use another counterweight, since the counterweight will be too heavy. Instead, a spring-based design is conceived [12]. Since the space around the third joint is quite limited, cables and pulleys were used such that the spring can be deployed at another place, as shown in Fig. 6(b).

Please note that the centroid of the gimbal structure may move in the horizontal direction during operation. It will be shown below that the change of the centroid position will not affect the gravity compensation of the third joint, due to the characteristics of the parallelogram structure. This property greatly facilitates the gravity compensation.

The force diagram of the parallelogram structure is presented in Fig. 6(a). The third active joint is indicated by point C, while the three passive joints are indicated by points A, B and D. The total mass of linkage BD, the gimbal structure and stylus is equivalent to a lumped mass m_F.

$f_{JI} = 2f_{cable}$ is the pulling force generated by the pulleys at points I and J, as shown in Fig. 6(b). f_{cable} is the tension in the cable that is routed to the springs.

Based on the virtual work principle, the third active joint's actuation torque M_{motor} required for the gravity compensation can be derived from (6).

$$M_{motor}\Delta q_3 - f_{JI}\Delta l_{JI} = m_{AB}g\Delta y_G + m_{CD}g\Delta y_H + m_F g\Delta y_F \quad (6)$$

Where l_{JI} is the distance between points J and I; y_G, y_H and y_F are the y-coordinates of point G, H and F; $\Delta y_G = l_{AG}\cos q_3\Delta q_3$, $\Delta y_H = l_{CH}\cos q_3\Delta q_3$, and $\Delta y_F = l_{CD}\cos q_3\Delta q_3$.

If the gravity is fully balanced, the motor at the third joint does not generate torque ($M_{motor} = 0$). Hence f_{JI} can be calculated from (7).

$$f_{JI} = -M_{const}\cos q_3\Delta q_3 / \Delta l_{JI} \quad (7)$$

Where $M_{const} = m_{AB}gl_{AG} + m_{CD}gl_{CH} + m_F gl_{CD}$.

Furthermore, Δl_{JI} is geometrically related to the joint value q_3 using (8).

$$l_{JI}^2 = l_{AI}^2 + l_{AJ}^2 - 2l_{AI}l_{AJ}\cos(\pi/2 - q_3)$$

$$\downarrow \text{ take the derivative of both sides} \quad (8)$$

$$l_{JI}\Delta l_{JI} = -l_{AI}l_{AJ}\cos(q_3)\Delta q_3$$

Combining (7) and (8), the f_{JI} can be expressed as in (9).

$$f_{JI} = \frac{M_{const}l_{JI}}{l_{AI}l_{AJ}} \quad (9)$$

f_{JI} is hence proportional to l_{JI} as the third active joint rotates. Two compression springs are deployed in the ParaMaster to generate the desired force f_{JI} as in (10).

$$f_{spring} = k\Delta l \quad (10)$$

Where k is the stiffness of the spring, and Δl is the deformation of the spring. As shown in Fig 6.(b), the relation of the length changes in the spring and between the points J and I is fixed with $\Delta l = \Delta l_{JI}/2$, due to the adopted design of using a pair of pulleys. The pre-compression of the springs is adjusted to generate $\Delta l = l_{JI}/2$. Then, the required stiffness k for the desired f_{JI} can be derived from (11).
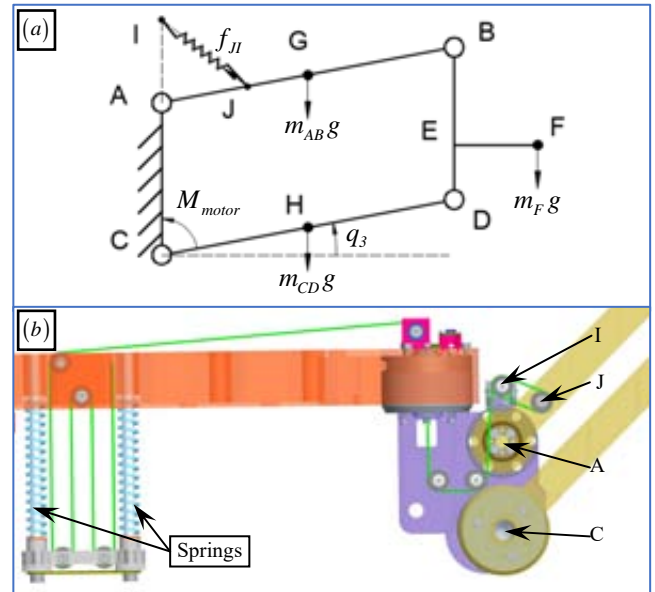

Fig. 6.(a) Force diagram of the parallelogram linkages; (b) gravity compensation of the third active joint

$$f_{cable} = f_{spring}/2$$

$$f_{JI}/2 = k\Delta l/2 \quad (11)$$

$$k = 2M_{const}/l_{AI}l_{AJ}$$

Two pulleys side by side installed at the point I, and one pulley installed at the point J are used to ensure that the cable under tension is not subject to sliding frictional wear. As shown in the left side of Fig. 6(b), pulleys are also applied to reduce the stroke of the spring, leading to a compact design.

Via the spring and the counterweight mentioned above, the gravity compensation design of the ParaMaster is achieved.

IV. DESIGN DESCRIPTION

In this section, the design description and the device

378

construction of the ParaMaster is reported in detail.

A. Structural Description

As shown in Fig. 7(a), the ParaMaster contains six active joints, three passive joints, and a stylus. All active joints are actuated by direct drive motors, for the sake of eliminating backlashes and reducing viscosity and friction caused by gearheads. The adopted direct drive motors all have hollow shafts, providing a channel for passing wires. The GM6020 motors (DJI Inc.) were used for the first, second and third joints, while two MC4310 motors and one MC3510 motor (Xunxue Inc., Guangdong, China) were used for the fourth, fifth, and sixth joints.

As depicted in Fig. 7(b), timing belts are used for the two direct drive motors of the two first joints of the left and right ParaMasters to increase the rated output torques by four times. Design compactness is realized by arranging the timing belts in a crossed manner.

The second joint is parallel to the first joint, with the stainless steel cables for gravity compensation passing through hollow shaft of the adopted GM6020 motor.

The parallelogram linkage is actuated by the third active joint to generate vertical translations. The orientation of the gimbal structure, attached at the distal side of the parallelogram structure, will not be tilted.

The total gravitational torque M_{const} is about 3200 mNm according to the CAD model. The stiffness of the springs were then calculated according to (11). Two compression springs (Tuhatsu Inc., Tokyo) were selected each with a stiffness of 3.7 N/mm.

The gimbal structure includes the last three active joints with their axes intersecting at the gimbal center.

A stylus is mounted on the distal side of the gimbal structure. There is a hand grip on the stylus, with a maximal open angle of 40°, which is used to control the open-close angle of the end effector of a slave surgical end effector (e.g., a needle driver).
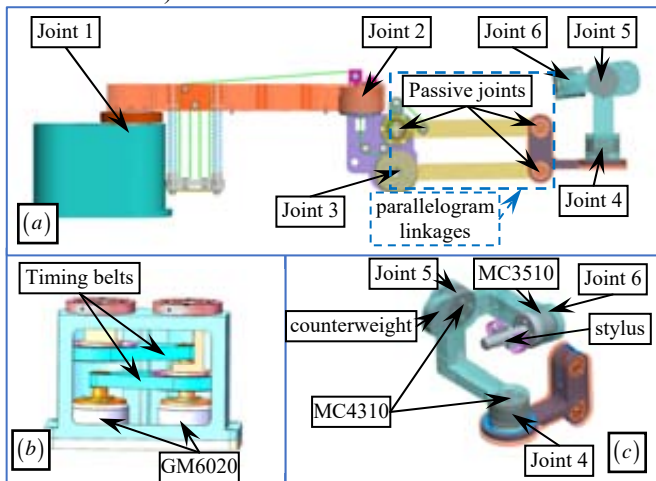

Fig. 7.The structural infrastructure of ParaMaster: (a) the ParaMaster; (b) the first active joints; and (c) the fourth, fifth and sixth active joints.

B. Control Infrastructure

As mentioned in Section IV.A, six direct drive motors are used in the ParaMaster. Three GM6020 motors are installed at the first three joints for the force output and angle sensing; Two MC4310 and one MC3510 motors are installed at the last three joints for the torque outputs and angle sensing. Each motor has a motor driver and a magnetic encoder integrated at the bottom of the motor.

The electronics diagram is shown in Fig. 8. The kinematics calculation and the data transmission are conducted in an RM57L843 development board (Texas Instrument, Inc.) with 330 Mhz CPU and 512 KB RAM, which is loaded with a FreeRTOS operating system for 2-ms control period. The communication bus between the controller and the motor drivers are the CAN (Controller Area Network) bus for the GM6020 motors, and the RS485 bus for the MC4310 and MC3510 motors, correspondingly.

The RM57L843 board sends torque commands to all six motors, while receiving angle readings from the motors. Then, various working modes of the ParaMaster can be realized.
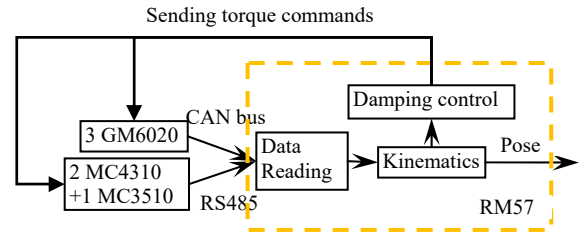

Fig. 8.Electronics diagram

V. EXPERIMENTAL CHARACTERIZATION

To verify the positioning input accuracy of the ParaMaster, the encoders of the direct drive motors are firstly calibrated as follows.

As shown in Fig. 9(a), a laser tracker system (AT403 from Leica Geosystems Inc.) was used to measure the position of a sphere marker as installed in Fig. 9(b). The sphere marker was connected to the motor via a 120 mm long acrylic bar. The acrylic bar is attached along the radial direction of the GM6020 motor to increase the resolution of the measured position. The position measured by the laser tracker has a volumetric accuracy of ±10 μm. For sake of brevity and without loss of genericity, only the calibration of the GM6020 motor is present as follows.

The motor was commanded to rotate from 0 to 8000 counts of its encoder, with a step of 200 counts. Each step is about 8.79°. During the calibration, the data of the encoder and the laser tracker were recorded simultaneously. The angle errors between the actual angle and the commanded angle can hence be plotted as shown in Fig. 10(a). A sine function is then formulated to fit the relation between the command encoder value E_v and the error angle ε as in (12).

$$\varepsilon = P\sin\left(\omega E_v + \varphi_0\right) + Q \tag{12}$$

Where P = -0.2177, ω = 0.0174, φ_0 = -0.3932, and Q = -0.004.

Using the fitted sine function, the calibrated results are shown in Fig. 10(b), where the angle errors are reduced to -0.3° to 0.2°. A possible explanation about this sinual errors in

379

Fig. 10(a) is that the GM6020 motor encoder is actually a magnetic one. The output number of counts are transmitted via analog to digital converstion.
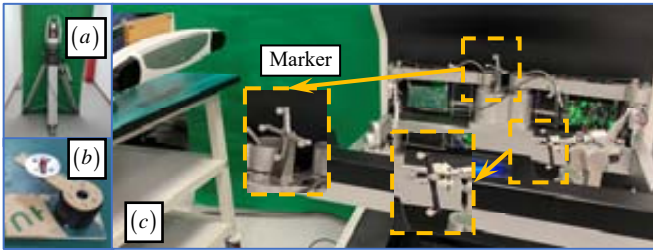

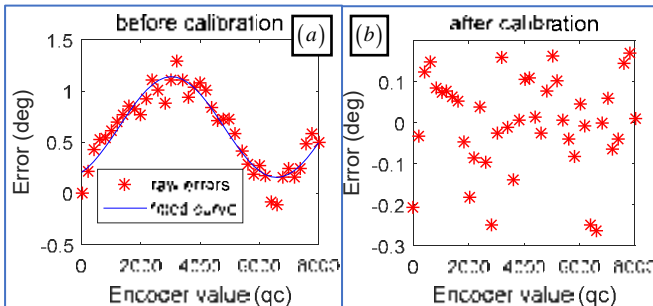Fig. 9.Experimental setup for the calibration and accuracy test

Fig. 10.Calibration of the encoder of the GM6020 motor (a) errors before calibration and fitted sine curve; (c) errors after calibration

Then, the testing setup for verifying the positioning input accuracy of the ParaMaster is shown in Fig. 9(c), where an optical tracker (Polaris Vega from Northern Digital Inc.) with two markers were used to measure the actual positions of the stylus. One marker was placed on the base of the ParaMaster, while the other one was fixed on the stylus. To test the accuracy of the ParaMaster, the corresponding proximal three joints were driven to 150 randomly generated values within the motion ranges, while the distal three joints were kept still. The positions measured by the Vega tracker gives a volumetric accuracy of 0.12 mm RMS.

As shown in Fig. 11, the average positioning error of the ParaMaster is 2.2 mm, with a maximum error of 7.3 mm. The errors were consistent with the results in Fig. 10(b), since 0.3° errors in the first three joints may correspond to a maximum positioning error of approximately 5.8 mm, with the structural parameters listed in Table I. Since this ParaMaster will be used in a vision-guided procedure, the errors may be actively corrected by a human operator during teleoperation.
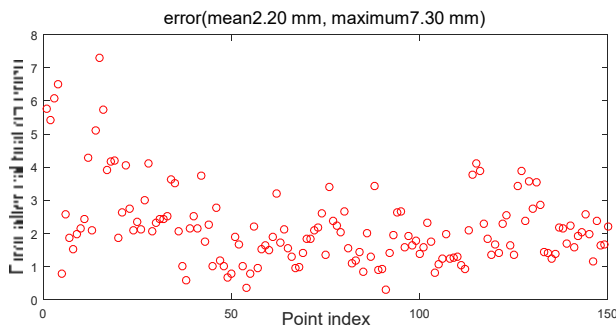

Fig. 11.Positioning errors of ParaMaster

VI. Conclusions and Future Work

This paper proposes a master haptic device with 6-DoF pose sensing and 6-DoF wrench outputs. Design concept, kinematics, dimension optimization, gravity compensation, system construction and preliminary experimental characteristization are reported in the paper.

In the proposed design, the direct drive motors are used for eliminating backlash and reducing resistance from the gear reducer. Furthermore, the use of the parallelogram structure contributes to the eased gravity compensation, a large workspace and simple kinematics.

After calibrating the motors' encoders, the ParaMaster achieved an average positioning accuracy of 2.20 mm in its workspace. The accuracy is expected to be improved by including other factors into consideration, e.g., the parts manufacturing tolerance and assembling alignment precision.

Other future works include the accuracy and response verification of the force and torque output capabilities, in both static and dynamic setting. Friction compensation shall also be investigated to diminish the movement resistance. Then, the ParaMaster is expected to be integrated into a surgical robotic system for teleoperated operations.

References

[1] R. H. Taylor, "A Perspective on Medical Robotics," *Proceedings of the IEEE,* Vol. 94, No.9, pp. 1652- 1664, 2006.

[2] A. M. Okamura, "Methods for Haptic Feedback in Teleoperated Robot-Assisted Surgery," *Industrial Robot: An International Journal,* Vol. 31, No.6, pp. 499-508, 2004.

[3] E. P. Westebring van der Putten, R. H. M. Goossens, J. J. Jakimowicz, and J. Dankelman, "Haptics in Minimally Invasive Surgery - a Review," *Minimally Invasive Therapy,* Vol. 17, No.1, pp. 3-16, 2008.

[4] B. Hannaford and A. M. Okamura, "Haptics," in *Springer Handbook of Robotics.* vol. Part D, B. Siciliano and O. Khatib, Eds.: Springer, 2008, pp. 719-739.

[5] J. Arata, H. Kondo, N. Ikedo, and H. Fujimoto, "Haptic Device Using a Newly Developed Redundant Parallel Mechanism," *IEEE Transactions on Robotics,* Vol. 27, No.2, pp. 201-214, 2011.

[6] G. Tholey and J. P. Desai, "A General-Purpose 7 DOF Haptic Device: Applications Toward Robot-Assisted Surgery," *IEEE/ASME Transactions on Mechatronics,* Vol. 12, No.6, pp. 662-669, Dec 2007.

[7] K. Kim and W. Kyun, "Design and Analysis of a New 7-DoF Parallel Type Haptic Device: PATHOS-II," in *IEEE/RSJ International Conference on Intelligent Robots and Systems (IROS),* 2003, pp. 2241-2246.

[8] E. L. Faulring, J. E. Colgate, and M. A. Peshkin, "The Cobotic Hand Controller: Design, Control and Performance of a Novel Haptic Display," *International Journal of Robotics Research,* Vol. 25, No.11, pp. 1099-1119, 2006.

[9] N. Bernstein, D. Lawrence, and L. Pao, "Dynamics Modeling for Parallel Haptic Interfaces with Force Sensing and Control," *IEEE Transactions on Haptics,* Vol. 6, No.4, pp. 429-439, 2013.

[10] G. Lee, S.-M. Hur, and Y. Oh, "A Novel Haptic Device with High-Force Display Capability and Wide Workspace," in *IEEE International Conference on Robotics and Automation (ICRA),* Stockholm, Sweden, 2016, pp. 2704-2709.

[11] G. D. Niemeyer, G. S. Guthart, W. C. Nowlin, N. Swarup, G. K. Toth, and R. G. Younge, "Camera Referenced Control in a Minimally Invasive Surgical Apparatus," Intuitive Surgical, Inc., 2002.

[12] V. A. Arakelian, "Gravity Compensation in Robotics," *Advanced Robotics,* Vol. 30, No.2, pp. 1-18, Nov 2015.